Key Points:
- High PAR transmittance (up to 0.41) through a refrozen lead compared to thicker snow-covered ice (<0.003)
- Ice algal biomass was similar in both ice types, despite greater light availability in the lead ice, possibly hampered by high irradiance
- High total MAA concentrations in the CDOM-low lead ice due to high light exposure

Windows in Arctic sea ice: Light transmission and ice algae in a refrozen lead

Hanna M. Kauko[1,2] iD, **Torbjørn Taskjelle**[3] iD, **Philipp Assmy**[1] iD, **Alexey K. Pavlov**[1] iD, **C. J. Mundy**[4], **Pedro Duarte**[1] iD, **Mar Fernández-Méndez**[1], **Lasse M. Olsen**[1] iD, **Stephen R. Hudson**[1] iD, **Geir Johnsen**[2], **Ashley Elliott**[4], **Feiyue Wang**[4], and **Mats A. Granskog**[1] iD

[1]Norwegian Polar Institute, Tromsø, Norway, [2]Trondhjem Biological Station, Department of Biology, Norwegian University of Science and Technology, Trondheim, Norway, [3]Department of Physics and Technology, University of Bergen, Bergen, Norway, [4]Centre for Earth Observation Science, University of Manitoba, Winnipeg, Manitoba, Canada

Abstract The Arctic Ocean is rapidly changing from thicker multiyear to thinner first-year ice cover, with significant consequences for radiative transfer through the ice pack and light availability for algal growth. A thinner, more dynamic ice cover will possibly result in more frequent leads, covered by newly formed ice with little snow cover. We studied a refrozen lead ($\leq$0.27 m ice) in drifting pack ice north of Svalbard (80.5–81.8°N) in May–June 2015 during the Norwegian young sea ICE expedition (N-ICE2015). We measured downwelling incident and ice-transmitted spectral irradiance, and colored dissolved organic matter (CDOM), particle absorption, ultraviolet (UV)-protecting mycosporine-like amino acids (MAAs), and chlorophyll *a* (Chl *a*) in melted sea ice samples. We found occasionally very high MAA concentrations (up to 39 mg m^{-3}, mean 4.5 ± 7.8 mg m^{-3}) and MAA to Chl *a* ratios (up to 6.3, mean 1.2 ± 1.3). Disagreement in modeled and observed transmittance in the UV range let us conclude that MAA signatures in CDOM absorption spectra may be artifacts due to osmotic shock during ice melting. Although observed PAR (photosynthetically active radiation) transmittance through the thin ice was significantly higher than that of the adjacent thicker ice with deep snow cover, ice algal standing stocks were low ($\leq$2.31 mg Chl *a* m^{-2}) and similar to the adjacent ice. Ice algal accumulation in the lead was possibly delayed by the low inoculum and the time needed for photoacclimation to the high-light environment. However, leads are important for phytoplankton growth by acting like windows into the water column.

1. Introduction

Arctic sea ice has changed rapidly over the last decades, from a predominantly thicker perennial to a seasonal and thinner ice cover, with implications for the whole Arctic marine system [e.g., *Meier et al.*, 2014]. The new ice-free areas have prompted an increase in phytoplankton primary production [*Arrigo and van Dijken*, 2015]. In ice-covered areas, thinning of the ice results in increased light availability in the visible range [*Nicolaus et al.*, 2012] and exposure to ultraviolet light [*Fountoulakis et al.*, 2014] for algae both associated with the ice (ice algae) and in the underlying water column (phytoplankton).

Dynamics of the Arctic ice cover are expected to increase, with accelerated motion of the thinner ice cover [*Kwok et al.*, 2013; *Itkin et al.*, 2017]. Leads are a ubiquitous feature of the Arctic ice cover, and the region north of Svalbard was identified as one with frequent occurrence of leads in the ice pack [*Willmes and Heinemann*, 2016], promoting formation of thin ice in the winter and spring. Despite relatively low coverage in the total ice pack, leads are important for the energy fluxes for the surrounding ice and the underlying water column [*Vivier et al.*, 2016; *Taskjelle et al.*, 2017]. Thin snow-free ice has high light transmittance: in an Arctic fjord (Kongsfjorden, Svalbard), 77–86% of incident light in the PAR range was transmitted through newly formed ice that accumulated ice algal biomass rapidly in a matter of days [*Taskjelle et al.*, 2016b].

Snow cover plays a critical role in the transparency of the sea ice cover and the resulting light field in and under the ice because it has a much stronger effect on light attenuation than the sea ice itself [*Grenfell and Maykut*, 1977; *Perovich*, 1990; *Hamre et al.*, 2004]. Thus, the snow cover influences the growth environment for sea ice algae. During early spring, primary production is light-limited and ice algal biomass is a negative function of snow depth [*Leu et al.*, 2015]. This relationship may reverse toward summer if the snow cover transmits enough light but delays bottom melt and the concomitant termination of the ice algal bloom and can protect ice algae from harmfully high irradiance levels [*Leu et al.*, 2015]. Under thin snow cover, the bottom ice community can

be sloughed off due to brine drainage and ice melt [*Mundy et al.*, 2005; *Campbell et al.*, 2014]. On the other hand, high ice algal standing stocks can increase ice melting due to increased energy absorption and heat dissipation, as shown in a modeling study by *Zeebe et al.* [1996]. The extent of algal-induced sea ice melting is dependent on the snow and ice thickness (i.e., the amount of light energy that reaches the algal layer) and the distribution of algae in the ice column. For example, an algal standing stock of 100 mg m^{-2} concentrated in bottom 4 cm of 140 cm thick ice could cause an ice thickness reduction exceeding the depth of the algal layer in just over a month, thus destroying the algal habitat [*Zeebe et al.*, 1996].

Light exposure can reach damaging levels and inhibit algal photosynthesis and growth. In snow removal experiments, decrease in ice algal biomass has been attributed to elevated light levels [*Juhl and Krembs*, 2010; *Campbell et al.*, 2015]. However, algae that were acclimated to high light (under initially thinner snow cover) coped well with the snow removal [*Juhl and Krembs*, 2010]. Algae have evolved several acclimation strategies to cope with and to utilize high irradiances, spanning different time scales (seconds to days). For example, several intracellular compounds, like photoprotective carotenoids of the rapid xanthophyll cycle, have been identified to shield excess light [*Brunet et al.*, 2011]. Protection from ultraviolet light (UVA: 320–400 nm, UVB: 280–320 nm) can be achieved with mycosporine-like amino acids (MAAs; reviewed in *Karentz* [2001], *Shick and Dunlap* [2002], and *Carreto et al.* [2011]).

MAAs are small water-soluble molecules that absorb in the UV range (in vitro absorption peaks range from 309 to 362 nm) and are efficient in dissipating the absorbed energy as heat. MAAs have also other roles in various organisms, like osmoregulation [cf. *Oren and Gunde-Cimerman*, 2007], but the photochemical and photophysical properties of, e.g., porphyra-334 support the suitability for photoprotection [*Conde et al.*, 2000]. Algae in sea ice with thin or no snow cover are potentially exposed to more harmful UV radiation than phytoplankton that is subject to vertical mixing in a deep water column. Antarctic diatoms have shown higher MAA production in an experimental light regime without mixing [*Hernando et al.*, 2011].

Composition of MAAs in sea ice algae has been reported to our knowledge only from two locations in the Northern Hemisphere: the Baltic Sea [*Uusikivi et al.*, 2010; *Piiparinen et al.*, 2015] and Allen Bay in the Canadian Arctic [*Elliott et al.*, 2015]. Reports from the Antarctic exist from McMurdo Sound [*Ryan et al.*, 2002] and Palmer station [*Karentz*, 1994]. MAA-like signatures have also been observed in particle absorption samples from sea ice [*Uusikivi et al.*, 2010; *Fritsen et al.*, 2011; *Mundy et al.*, 2011; *Piiparinen et al.*, 2015; *Taskjelle et al.*, 2016b]. Likewise, MAA-like absorption peaks in the UV range have been observed in the dissolved matter fraction of melted sea ice samples [*Uusikivi et al.*, 2010; *Xie et al.*, 2014; *Logvinova et al.*, 2016; *Taskjelle et al.*, 2016b]. Besides MAAs, other algal pigments and colored dissolved organic matter (CDOM) significantly affect light absorption in the ice [*Perovich et al.*, 1998; *Belzile et al.*, 2000; *Uusikivi et al.*, 2010].

Here we present a unique spring time series of bio-optical properties in young sea ice in a refrozen lead from the Norwegian young sea ICE expedition (N-ICE2015). The N-ICE2015 expedition consisted of a nearly half-year long field campaign with drifting ice stations between 80° and 83°N in the southern Nansen Basin of the Arctic Ocean [*Granskog et al.*, 2016], with the aim to study the energy fluxes and state of the ice-associated ecosystem in the new, thinner Arctic sea ice regime. Little is known about the radiative processes in newly formed sea ice [cf. *Taskjelle et al.*, 2016b] and the suitability of young ice as a habitat, which limits our understanding of how the Arctic marine ecosystem will respond to a thinner and more dynamic ice cover in the future Arctic Ocean. *Steiner et al.* [2016] pointed out that in biogeochemical sea ice modeling there is a need for better understanding of the radiative transfer processes. The striking feature of the young ice environment is the high irradiance due to thin ice and snow cover and its potential effects on ice algae. The objectives of this study were to investigate light transmission through young sea ice and to assess the optical properties of the algal biomass growing in this type of ice. For this we characterized the absorption properties and the UV-protecting pigments (MAAs) of ice algae. To determine and disentangle the role of dissolved and particulate matter in light absorption in thin ice, we conducted a case study on light transmittance with a radiative transfer model.

2. Materials and Methods

2.1. N-ICE2015 Expedition

During the N-ICE2015 expedition research vessel *Lance* was frozen into pack ice north of Svalbard between January and June 2015 [*Granskog et al.*, 2016]. In total, four ice floes were monitored during the study period
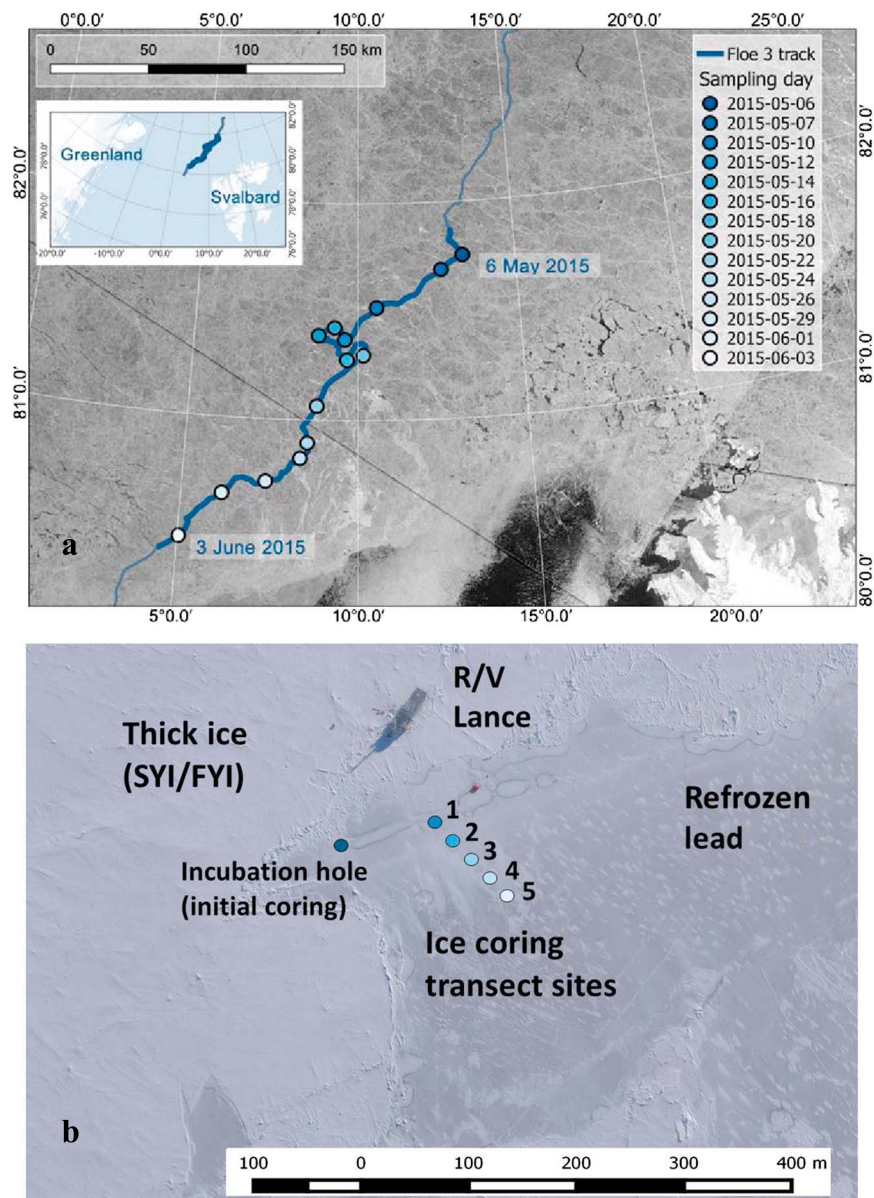
Figure 1. (a) Drift trajectory of Floe 3 of N-ICE2015 expedition north of Svalbard (satellite image taken on 25 May). The sampling period with start and end dates is marked in bold on the drift trajectory, and the sampling days are indicated with circles (see legend). Image source: RADARSAT-2 image provided by NSC/KSAT under the Norwegian-Canadian RADARSAT agreement. RADARSAT-2 Data and Products © MacDonald, Dettwiler and Associates Ltd (2013) All Rights Reserved. RADARSAT is an official mark of the Canadian Space Agency. Map created by the Norwegian Polar Institute/Max König. (b) Aerial image of the refrozen lead and R/V *Lance* (image taken on 23 May 2015) and location of sampling sites. Image: Vasily Kustov and Sergey Semenov (Arctic and Antarctic Research Institute, St. Petersburg, Russia).

to investigate the thinning Arctic ice pack. This paper presents data from the drift of Floe 3 [see *Granskog et al.*, 2016], studied from mid-April to early June, and specifically focuses on data from a refrozen lead during this part of the drift (80.5–81.8°N; Figure 1).

2.2. Sampling on the Refrozen Lead

A lead (approximately 400 m wide) that opened close to the vessel on 23 April began to refreeze on 26 April and was completely refrozen by 1 May. The young ice that formed in the lead was sampled from 6 May, when

ice had grown 15 cm thick and was safe to work on, until it broke up on 4 June. From 7 May onward, a 100 m long sampling transect was established from the edge of the lead toward its center (Figure 1b), when ice thicknesses were 17–24 cm. The transect was sampled every 2–3 days (13 times in total) between 7 May and 3 June 2015 (see Table S1; Figure 1a).

On the refrozen lead, incoming (planar downwelling) and ice-transmitted spectral irradiance ($E_d(\lambda)$) were simultaneously measured with two Ramses ACC-VIS spectroradiometers (TriOS Mess- und Datentechnik GmbH, Rastede, Germany) for the wavelength range 320–950 nm, at five locations along the transect, 25 m apart from each other (Figure 1b). Data are available in *Taskjelle et al.* [2016a]. On three occasions (see Table S1), measurements were repeated after snow was carefully removed with a shovel within a radius of about 1 m around the location of the under-ice sensor. The radius is a sufficient distance to avoid edge effects from snow cover, according to *Petrich et al.* [2012]. All sensors were factory calibrated shortly before the field campaign. Field comparisons of the different sensors suggest an uncertainty on the order of ±10% in measured energy fluxes in the UV range, due to calibration uncertainties under variable incident light fields. For under-ice measurements, a hinged arm placing the sensor 1 m away from the initial 9 cm hole was used. Measurements with a tilt less than 5° were used (3–10 spectra were averaged). Spectral irradiance was converted from W m^{-2} nm^{-1} to µmol photons m^{-2} s^{-1} for E_d(PAR). After the transmittance measurements snow depth was measured (an average of 5–10 locations within 1 m from the under-ice sensor site).

After snow depth recordings, two (until 16 May) or three (18 May onward) 9 cm diameter ice cores were collected with an ice corer (Mark II coring system, KOVACS enterprise, Roseburg, USA) at the site of the under-ice sensor and combined into one melting bucket. Occasionally, additional cores for ice stratigraphy and temperature were collected (Table S1). Ice temperature data are available in *Gerland et al.* [2017]. Brine salinity was calculated from ice temperatures based on *Cox and Weeks* [1986] for temperatures < -2°C and *Leppäranta and Manninen* [1988] for temperatures > -2°C. From 18 May onward, cores were cut into two sections: bottom 10 cm and the top (rest of the core: 9–17 cm). On a subsequent new sampling day, the transect was moved on average 2–3 m away from the earlier transect line, to measure transmittance and collect cores at an undisturbed location.

Ice cores were brought back onboard in darkness and melted overnight at room temperature without addition of filtered seawater [cf. *Rintala et al.*, 2014]. The melting buckets were monitored to sample the buckets as soon as the ice had melted. Samples for fluorometric chlorophyll *a* (Chl *a*), particle absorption (a_p), and MAAs were filtered onto Whatman GF/F filters (diameter 25 mm; GE Healthcare, Little Chalfont, UK) under low vacuum pressure (ca −30 kPa) and shading from excess light. MAA and a_p samples were stored at −80°C until analysis. Colored dissolved organic matter (CDOM) samples were filtered through a 0.2 µm PALL Acrodisc syringe filter (PALL Corporation, Ann Arbor, USA) with acid-washed all-plastic syringes into precombusted amber glass vials and stored at +4°C in the dark. Salinity in the melted samples was measured with WTW Cond 3110 probe (WTW Wissenschaftlich-Technische Werkstätten GmbH, Weilheim, Germany). Ice core data (other than absorption spectra) are available in *Assmy et al.* [2017b].

For continuous incident spectral downwelling irradiance measurements Ramses ACC-VIS spectroradiometers (TriOS Mess- und Datentechnik GmbH, Rastede, Germany) were used [*Taskjelle et al.*, 2016a]. Measurements were performed at a fixed location on the adjacent second-year ice (initial ice thickness 130 cm, snow depth 40 cm) throughout the period the refrozen lead was sampled. At the same site, another sensor recorded the under-ice irradiance [*Taskjelle et al.*, 2016a].

2.3. Laboratory Analysis of Ice Core Samples

Chl *a* was extracted with 100% methanol at 5°C for 24 h [*Holm-Hansen and Riemann*, 1978] and measured fluorometrically using a Turner 10-AU Fluorometer (Turner Designs, San Jose, USA).

Particle absorbance was measured between 240 and 800 nm with a Shimadzu UV-2450 dual-beam spectrophotometer with an integrating sphere (ISR-2200, Shimadzu Corporation, Kyoto, Japan) following the modified method described in *Tassan and Ferrari* [2002] and recommendations in *Tilstone et al.* [2002] and *Mueller et al.* [2003]. The diameter of the colored area on the filter was measured on each sample individually. As a wet reference, an average of 20 blank filters, prepared with ultrapure water in the field throughout the campaign, was used to account for light scattering and absorption by the filter. Filters were bleached with

400 µL of sodium hypochlorite (NaClO with 1% active chlorine) for 10 min, with additional 20 min if first bleaching was not complete and rinsed with 30 mL of artificial seawater (60 g Na_2SO_4 in 1 L of ultrapure water). Optical density (absorbance) of particles on filters ($OD_s(\lambda)$) was converted to optical density of particles in suspension ($OD_{sus}(\lambda)$) following equation 10 in *Tassan and Ferrari* [2002]

$$OD_{sus}(\lambda) = 0.423 \times OD_s(\lambda) + 0.479 \times OD_s(\lambda)^2 \tag{1}$$

$OD_{sus}(\lambda)$ was then converted to an absorption coefficient $a_p(\lambda)$:

$$a_p(\lambda) = 2.303 \times OD_{sus}(\lambda)/l \tag{2}$$

where 2.303 is the natural logarithm of 10, and l is the hypothetical path length in meters, based on the ratio between the filtered sample volume and sample area diameter on the filter. A baseline correction was done relative to the mean absorption values at 750–800 nm.

Measurement before bleaching yields the total particle absorption (a_p, m^{-1}), whereas spectra after bleaching show detrital (nonpigmented particles) absorption (a_d, m^{-1}). Difference between these is the algal (pigment) absorption (a_ϕ, m^{-1}). Dividing a_ϕ by the corresponding Chl a values (in mg m^{-3}) gives Chl a-specific algal absorption (a_ϕ^*, m^2 (mg Chl)$^{-1}$). Particle spectral absorption coefficients are available in *Kauko et al.* [2017].

CDOM absorbance was measured between 240 and 700 nm with 0.5 nm resolution using a Shimadzu UV-2401PC spectrophotometer (Shimadzu Corporation, Kyoto, Japan) and 10 cm quartz cells with fresh ultrapure water as reference. Absorbance values were baseline corrected following *Stedmon et al.* [2000], using a constant that accounts for minor shifts at longer wavelengths. Absorbance values were then converted to an absorption coefficient a_{CDOM} (m^{-1}) following

$$a_{CDOM}(\lambda) = 2.303 \times A(\lambda)/l \tag{3}$$

where $A(\lambda)$ is the absorbance at a given wavelength λ and l is the path length of the cuvette in meters. CDOM spectral absorption coefficients are available in *Pavlov et al.* [2017a].

MAA analysis by high-performance liquid chromatography (HPLC) in the Ultra-Clean Trace Elements Laboratory (UCTEL) at the University of Manitoba (Winnipeg, Canada) is described in *Elliott et al.* [2015] and based on the method by *Carreto et al.* [2005]. In short, samples were extracted with 100% methanol then evaporated to dryness and reconstituted with the starting mobile phase (0.2% formic acid in water adjusted to pH = 3.15). Analysis was done with a HPLC (Agilent 1200)-electrospray ionization (ESI)-triple quadrupole mass spectrometer (MS) (Agilent 6410b) (i.e., HPLC-ESI-MS) coupled with a diode array and multiple wavelength detector (Agilent 1100 series; Agilent technologies, Santa Clara, USA). Although a number of MAAs were detected in the samples, structural identification and quantification were only possible for shinorine, palythine, and porphyra-334 for which standards were available [*Elliott et al.*, 2015]. Total MAA concentration reported herein refers to the sum of these three components only and thus underestimates the total MAA concentration.

The procedure we used for the stratigraphy ice cores is described in more detail in *Olsen et al.* [2017] and based on the method described in *Lange* [1988]. In short, the vertical surface of the ice core section was smoothed with a microtome. Thick sections (5–7 mm) were photographed in normal light and thin sections (1 mm) in polarized light to examine air pockets, brine channels, and ice crystal structure.

2.4. Radiative Transfer Model

We applied the AccuRT radiative transfer model [*Hamre et al.*, 2017] to investigate the effect of various constituents on light attenuation in the UV and PAR range in the ice. AccuRT is a 1-D coupled atmosphere-snow-ice-ocean model based on DISORT [*Thomas and Stamnes*, 1999]. The model has been used successfully for atmosphere-snow-sea ice-ocean work by, e.g., *Hamre et al.* [2004] and on thin ice by *Taskjelle et al.* [2016b]. In this study, the atmosphere contained a 500 m thick cloud layer where volume fraction and particle size were adjusted so that the measured incident irradiance was reproduced well. The zenith angle was set to 60°, representative of time of day and location of irradiance measurements. Modeled albedo was somewhat higher (10% for snow-covered case, 20% for bare ice) than

Table 1. Descriptions of Model Components[a]

Model Component	Explanation
Observed with snow	Measured in situ transmittance
Observed without snow	Measured in situ transmittance after snow removal
Pure sea ice	Ice with brine and bubbles but without organic and inorganic matter (CDOM and particles)
Ice	Ice with brine, bubbles and matter (CDOM and/or particles) that is specified in the legend entry
Snow	The observed 2 cm snow cover
CDOM	Measured ice core sample CDOM absorption spectra
CDOM$_{exp}$	Exponential CDOM spectra; measured spectra without MAA peaks
CDOM$_{Baltic}$	CDOM absorption spectrum from Baltic Sea ice
Particles	Particle absorption (algal and nonalgal particles)

[a]Each modeling case was a combination of the different components listed.

measured, modeled absorption is thus a conservative estimate. Snow was represented by a layer of ice spheres with a radius of 170 μm and density of 205 kg m^{-3} added to the bottom of the atmosphere, with inherent optical properties (IOPs) computed using a parameterization based on Mie code [*Stamnes et al.*, 2011]. The values were chosen for optimal transmittance reproduction but are near what was measured on the refrozen lead (optical radius of snow grains 190 μm; no density measurements on 26 May but the density on 29 May was 160 kg m^{-3}; J.-C. Gallet, personal communication, 2016). The thickness of the layer was the same as the measured snow depth (2 cm). Layers containing ice in the model were specified based on the sectioning of the ice cores, i.e., a lower layer that is 10 cm thick and an upper layer that covers the remaining ice thickness. Absorption coefficients of pure ice are from *Warren and Brandt* [2008]. For pure water, absorption coefficients are from *Mason et al.* [2016] and *Pope and Fry* [1997]. Photos of thick sections indicated larger brine pockets and higher brine volume fraction in the granular ice than in the columnar ice. Brine is represented as spheres of water, and following the observations from the thick sections, we set the brine volume to 30% and 10% in the granular and columnar layers, respectively, and the radius to 1 mm and 0.3 mm. The air bubble radius was set to 0.1 mm in both layers, and the air volume fraction was adjusted until modeled transmittance had a good fit with the measured transmittance. It is assumed that the layers are uniform. With 0.85% air in the granular layer and 0.3% in the columnar layer, effective scattering coefficients ($b_{eff} = b(1 - g)$, where g is the average cosine of the scattering angle) were about 20 m^{-1} and 8 m^{-1}, respectively. As for the snow, IOPs are obtained using the parameterizations defined by *Stamnes et al.* [2011] based on the size and volume fraction of the inclusions. Absorption coefficients corresponding to the measured absorption by particulate and dissolved matter (Figure 3h) were added to the ice. Measured spectral absorption and scattering coefficients in the water column [*Pavlov et al.*, 2017b; *Taskjelle et al.*, 2017] were used for the layer describing the water column below the ice. The components used in and on the ice are listed in Table 1.

3. Results

3.1. Physical Environment

Subzero air temperatures and cloudy skies prevailed during the lead sampling period (6 May to 3 June) [*Hudson and Cohen*, 2015; *Cohen et al.*, 2017; *Walden et al.*, 2017]. Until 24 May, air temperature ranged between −20 and −10°C, except for two days (16 and 19 May) when temperatures rose to around 0°C. Both days were associated with a single large-scale storm event [*Cohen et al.*, 2017]. From 24 May onward, temperatures were between −10 and 0°C [*Cohen et al.*, 2017; *Hudson and Cohen*, 2015]. Cloud fraction was often >0.9 [*Walden et al.*, 2017]. On six days (6, 8, 12, and 22 to 24 May) lower fractions were observed (0–0.64). Ocean Conservative Temperature [*McDougall et al.*, 2012] under ice (2 m depth) was between −1.60 and −1.87°C during the sampling period, nearly at freezing temperature [*Meyer et al.*, 2017].

Ice thickness during transect sampling ranged between 17 and 27 cm (Figure 2a). Ice thickness at sites 2–5 was within a few centimeters of each other, while site 1 was the thinnest throughout. Ice growth was observed in the beginning of the sampling, but after 20 May a reduction in thickness due to ice melt was
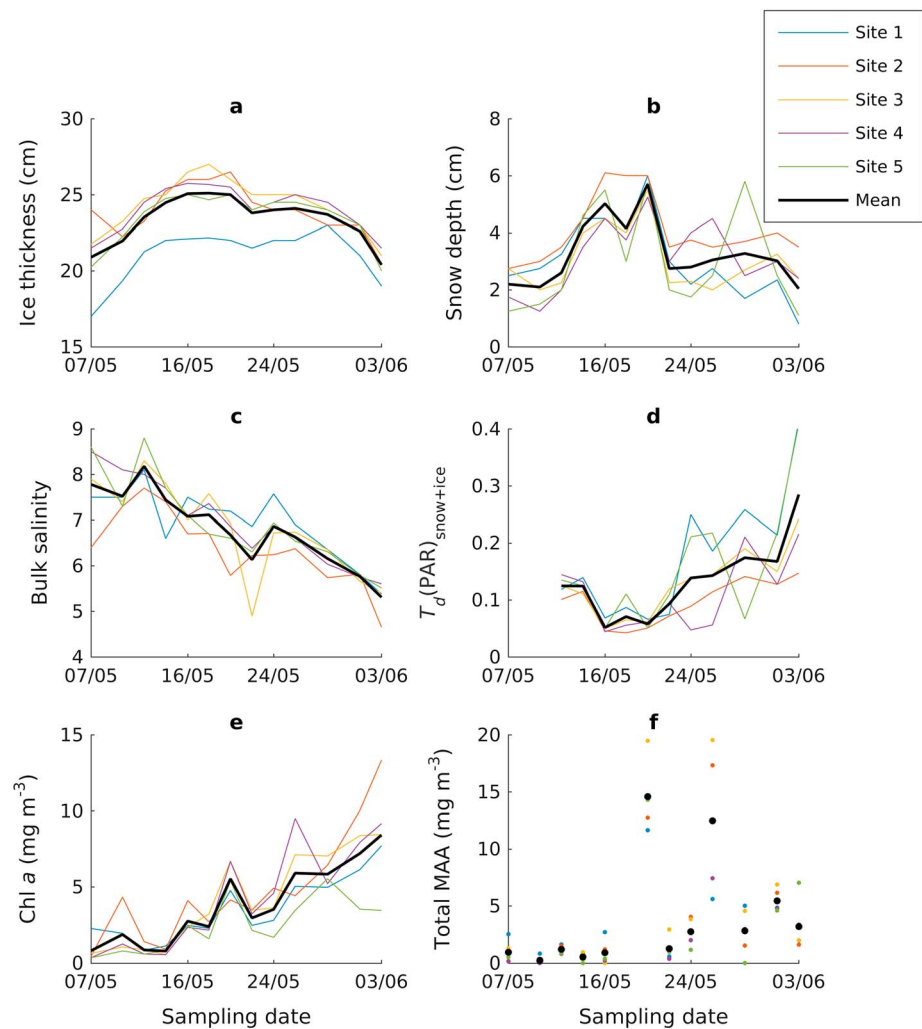
Figure 2. Time series of (a) ice thickness, (b) snow depth, (c) bulk salinity, (d) E_d(PAR) transmittance through snow and ice ($(T_d$(PAR)$)_{snow+ice}$), (e) Chl a, and (f) total MAA concentration (shinorine, palythine, and porphyra-334) for the five different coring sites on the refrozen lead, including the mean (black line or black dots). In the case of bulk salinity, Chl a, and MAAs the mean values after 18 May are volume-weighed means of the core top and bottom values. There are no data for transmittance for the first two days (7 and 10 May) and for MAA on 18 May.

observed at all sites. After 22 May ice grew slightly, but during the last week of sampling ice was continuously melting. The ice consisted of a granular ice layer on the top and columnar ice at the bottom (not shown), but the relation between granular and columnar ice was different between the sites. On 26 May, sites 1 and 5 had 4–5 cm granular ice and 17–19.5 cm of columnar ice, compared to 17 cm of granular and 5–8 cm of columnar ice at sites 2 and 3. Site 4 had 12 cm granular and 12.5 cm columnar ice.

Snow depth ranged from 1 to 6 cm (Figure 2b). The deepest snow cover (4 to 6 cm) was observed between 14 and 20 of May, concurrent with snowfall events during 16 and 19 May. After 20 May, snow depth decreased to 2–3 cm, likely due to wind redistribution. In the beginning, the refrozen lead was covered by frost flowers that were then covered by snow. Later in the sampling, the snow pack developed a surface crust of melt grain clusters and later a wind slab. The bottom of the snow pack was first characterized by loose snow, later wet, and salty depth hoar (possibly remnants of the frost flowers) or slush.

Mean sea ice bulk salinity decreased during transect sampling period from 7.8 to 5.3 (Figure 2c). Brine salinity (calculated from ice temperature) ranged between 23.9 and 52.2 during transect sampling (18 May to 1 June). On 6 May, before the transect sampling started, brine salinity was up to 78.9 in the top 3 cm of the ice core and ice temperature was −4.45°C.
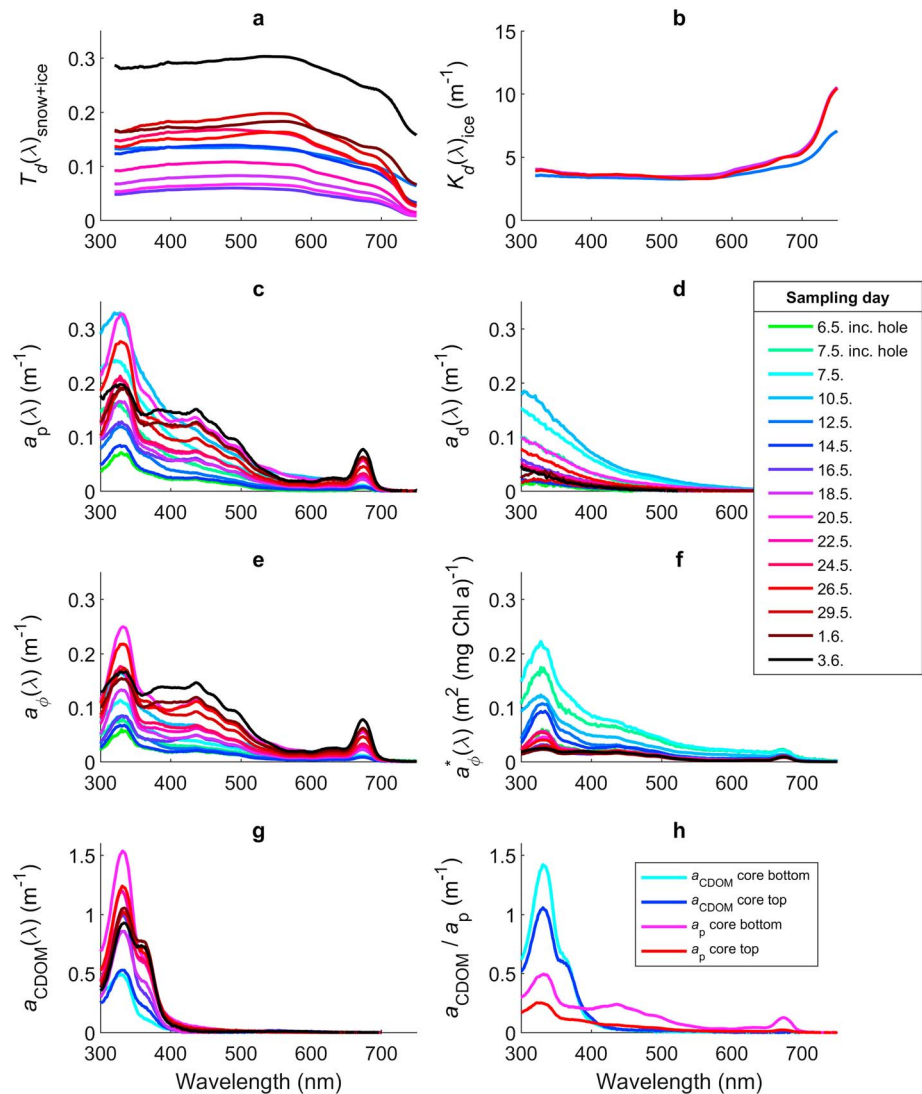
Figure 3. Absorption and diffuse attenuation coefficients and spectral transmittance in the refrozen lead. (a) Measured spectral transmittance through snow and ice. (b) Diffuse attenuation coefficients ($K_d(\lambda)_{ice}$) for ice, calculated from incoming and ice-transmitted irradiance measurements after snow removal. Absorption by particles, for (c) total (a_p), (d) detritus (a_d), and (e) algal (a_ϕ) particles. (f) Chl a-specific absorption of algae (a_ϕ^*). (g) CDOM absorption (a_{CDOM}). (h) CDOM and particle absorption spectra on 26 May on site 3. All transect spectra are averages of the five sites on the corresponding day, except in Figure 3h (only site 3). In Figures 3c–3f, the data labeled "inc. hole" (incubation hole) on 6 and 7 May are from another coring location on the lead that was sampled prior to the transect (see map in Figure 1b), with two cores averaged on 6 May and three cores averaged on 7 May. Other legend entries refer to transect sampling dates. Measurements from 12 May onward are included in Figure 3a, from 12, 18, and 26 May in Figure 3b, from all dates in Figures 3c–3f, and from all dates but 10 and 12 May in Figure 3g. From 18 May onward, values in Figures 3c–3g are volume-weighed means of the ice core top and bottom values.

Measured incoming E_d showed a distinct diurnal pattern and a slight increase from early May to early June (Figure S1), with maximum values of 1240 µmol photons m^{-2} s^{-1} for E_d(PAR) and 80 µmol photons m^{-2} s^{-1} for E_d(UV$_{350-400}$) (UV light integrated over 350–400 nm) [*Taskjelle et al.*, 2016a]. Mean E_d(PAR) values in the 48 h prior to sampling ranged between 450 and 730 µmol photons m^{-2} s^{-1} (Figure S2).

3.2. Light Transmission Measurements

Transmittance T_d(PAR)$_{snow+ice}$, the fraction of E_d(PAR) transmitted through snow and ice, was 0.05−0.41 and inversely related to snow depth (Figures 2b, 2d, and S3). Spectral transmittance, $T_d(\lambda)_{snow+ice}$, is shown in Figure 3a. Measured E_d(PAR) under the snow-covered thin ice ranged between 30 µmol photons m^{-2} s^{-1}

and 350 μmol photons $m^{-2}\,s^{-1}$. To study transmittance through bare ice, snow was carefully removed and the irradiance measurements were repeated for snow-free ice on three sampling days (12, 18, and 26 May). While it is impossible to completely remove the effect of a snow cover, the level and salty ice surface made the conditions on the lead as ideal as possible, and we are confident that any remaining snow had very little effect on the measurements. $T_d(PAR)_{ice}$ for snow-free ice ranged from 0.28 to 0.49. Sites 1 and 5 had the highest snow-free transmittance on all days, and sites 2 and 3 the lowest. Transmittance after snow removal was 2.2–6.5 times higher than transmittance through snow-covered ice on the corresponding site and day. E_d(PAR) values under snow-free ice ranged between 225 and 420 μmol photons $m^{-2}\,s^{-1}$.

The diffuse attenuation coefficient $K_d(PAR)_{snow+ice}$ for snow and ice was calculated from the downwelling and transmitted $E_d(PAR)$ using the equation

$$K_d(PAR)_{snow+ice} = \frac{1}{z}\ln\left[\frac{E_d(0,PAR)}{E_d(z,PAR)}\right] \tag{4}$$

where z is the total thickness of snow and ice, E_d(0,PAR) is downwelling irradiance above ice and snow, and E_d (z,PAR) downwelling irradiance right below the ice. $K_d(PAR)_{snow+ice}$ ranged from 4.5 to 12.4 m^{-1}. Using the measurements after snow removal, we calculated K_d of the sea ice, both spectrally ($K_d(\lambda)_{ice}$) and for the PAR range (z is the total thickness of ice, and E_d(0) downwelling irradiance above ice). Specular reflection of 5% ($R_s = 0.05$) was introduced following *Ehn et al.* [2004].

$$K_d = \frac{1}{z}\ln\left[(1-R_s)\frac{E_d(0)}{E_d(z)}\right] \tag{5}$$

Both $K_d(\lambda)_{ice}$ (Figure 3b) and $T_d(\lambda)_{snow+ice}$ (Figure 3a) show signs of algal pigment absorption at 674 nm especially later in the sampling period. $K_d(PAR)_{ice}$ ranged between 2.9 and 4.7 m^{-1} (median and mean 3.7 m^{-1}). Based on the $K_d(PAR)_{ice}$ and the $E_d(PAR)$ measurements with snow, $K_d(PAR)_{snow}$ for snow was calculated as follows:

$$K_d(PAR)_{snow} = -\ln\left[\frac{E_d(z,PAR)}{E_d(0,PAR)\times\exp(-K_d(PAR)_{ice}\times z_{ice})}\right]/z_{snow} \tag{6}$$

where z_{ice} and z_{snow} are the ice and snow thickness, respectively. $K_d(PAR)_{snow}$ ranged between 21.2 and 63.7 m^{-1} (median 39.2 and mean 43.1 m^{-1}).

3.3. Biomass and Bio-optical Properties

The ice algal biomass, measured as Chl *a* standing stock, increased with time. Standing stocks in the lead were 0.06–2.31 mg Chl *a* m^{-2} and Chl *a* concentration 0.33–13.33 mg Chl *a* m^{-3} (Figure 2e). Between 20 and 22 May all sites experienced a distinct reduction in Chl *a*. Most ice algal biomass was concentrated in the ice core bottom sections (Figure 4a).

In general, total particle (a_p) and algal absorption (a_ϕ) in the PAR range increased during the study period (Figures 3c, 3e, 5a, and 5b). Values of a_ϕ at 440 nm (absorption peak of Chl *a* and contribution from other pigments) ranged between 0.015 and 0.390 m^{-1} for individual samples (Figure 3 shows averages of the five transect sites and after 18 May volume-weighed mean values of ice core top and bottom sections). In contrast, Chl *a*-specific algal absorption (a_ϕ^*) was highest in the beginning of the sampling period and then decreased (Figure 3f). Values of a_ϕ^* at 440 nm ranged between 0.013 and 0.099 m^2 (mg Chl *a*)$^{-1}$. Early days of the transect sampling show highest detrital absorption (a_d), up to almost 0.18 m^{-1} at 300 nm on average (Figure 3d). To assess the variability along the transect, we calculated the coefficient of variation (CV) at 440 nm for lead transect days: CV for a_p, a_d, a_ϕ, and a_ϕ^* was 10–63, 12–73, 11–67, and 10–61%, respectively. From 12 May onward, CV at 440 for a_p, a_ϕ, and a_ϕ^* was smaller, 10–34, 11–35, and 10–31%, respectively.

The samples collected on 20 and 26 May stand out with high absorption (and biomass, Figure 2e). All spectra show strong absorption in the near-UV range (300–400 nm). Especially in the core tops (Figures 5b and 5d), absorption in UV range is high compared to the PAR range. Toward the end of the sampling, the peak at 380 nm increased relative to the peak at 330 nm (Figure 4d).
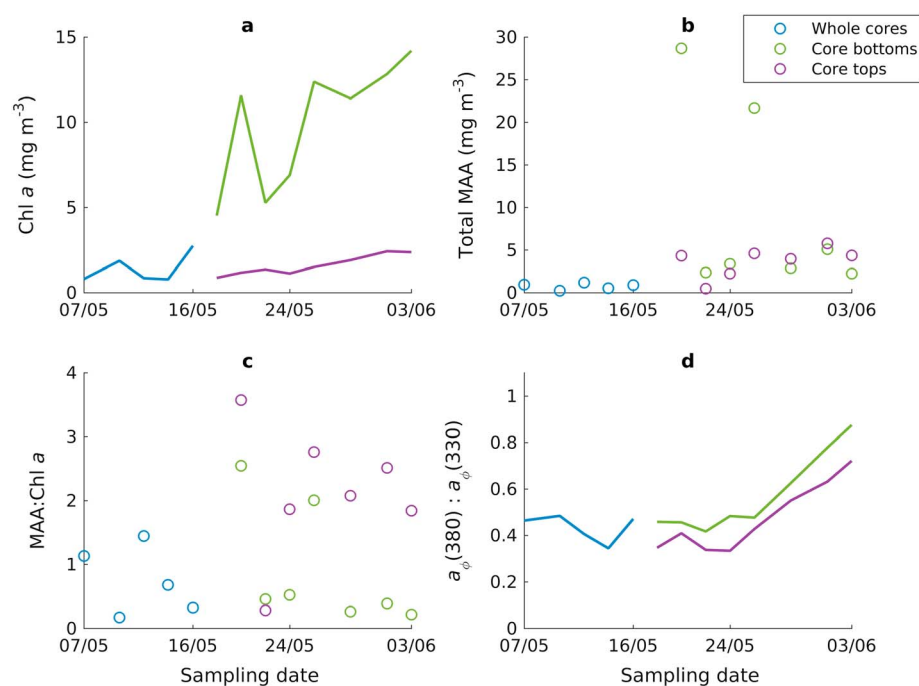
Figure 4. Time series of Chl a and MAA concentration for ice core bottom and top sections (average of five sites). Until 16 May, the ice core was sampled as one ("whole cores"). Core sectioning was started on 18 May, after which the ice core was sampled in two separate sections ("core bottoms" and "core tops"). (a) Chl a, (b) total MAA concentration, (c) MAA to Chl a ratio, and (d) ratio between algal absorption (a_ϕ) at 380 nm to that at 330 nm.

CDOM absorption at 295 nm ranged between 0.18 and 1.53 m^{-1} for individual samples. All CDOM samples show very high absorption in the near-UV range (peaks at 330 and 360 nm) (Figure 3g). Difference in the shape of the spectra between ice core bottom and top samples is visible (Figures 5e and 5f): a second peak, at 360 nm, becomes gradually more prominent in the core tops. Absorption values are otherwise similar.

In general, the total MAA concentration (shinorine, palythine, and porphyra-334) increased over time (Figure 2f). Two days, 20 and 26 May, stand out with high concentrations: up to almost 20 mg MAAs m^{-3} for the whole ice column (a volume-weighed mean of ice core bottom and top samples). The highest concentration (39 mg m^{-3}) was measured in an ice core bottom sample from 26 May. Mean concentration of all samples ($n = 92$) was 4.5 ± 7.8 mg m^{-3}. The difference between ice core bottom and top sections is shown in Figure 4b. The MAA to Chl a ratio (mg MAA m^{-3} to mg Chl a m^{-3}) was higher in the core tops with the exception of 22 May and ranged on average (average of five sites) up to 3.6 (Figure 4c) and for all samples up to 6.3 on 20 May (mean 1.2 ± 1.3, $n = 92$). The patterns in concentration were similar for the three individual MAAs (individual plots not shown). Shinorine was the most abundant compound, followed by porphyra-334 and then palythine. In addition to the three compounds that could be verified with standards, two unknown ones were observed: one with the absorption maximum at 331 nm and retention time of 18.0 min was abundantly present in most of the samples. This compound is likely mycosporine-serine-glycine methyl ester [*Carignan and Carreto*, 2013], based on mass spectrometer results. Based on estimated concentration using the molar extinction coefficient of the related shinorine [*Karentz*, 2001], this compound contributed on average 62 ± 25% to the total concentration of these four compounds. Another unknown compound that corresponds to U2 in *Elliott et al.* [2015], with the absorption maximum at 363 nm and a secondary peak at 337 nm, was present mainly on 20 and 29 May.

3.4. Contribution of the Different Components to Light Absorption

As a case study to investigate the role of particulate and dissolved matter for light transmittance, we used data from site 3 on 26 May and compared radiative transfer model results to measured transmittance. On this day and site, the measured snow cover was 2 cm and the observed T_d(PAR) was 0.15 and 0.32 for the ice with
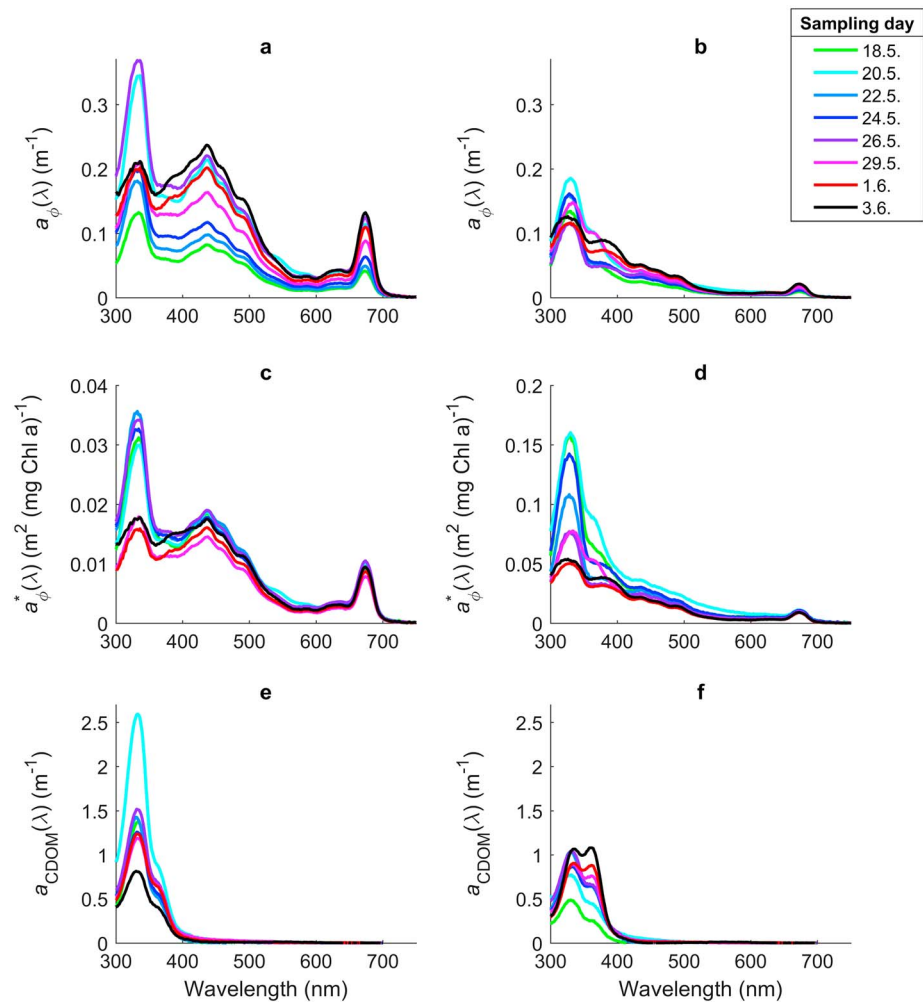
Figure 5. Absorption spectra in ice core bottoms (Figures 5a, 5c, and 5e) and tops (Figures 5b, 5d, and 5f). (a, b) Algal absorption (a_ϕ), (c, d) Chl a-specific algal absorption (a_ϕ^*), and (e, f) CDOM absorption (a_{CDOM}) coefficients. Note different scales on y axis between Figures 5c and 5d.

and without snow, respectively. Transmittance was largest at 558 nm in both cases. Modeled T_d(PAR) with all constituents was 0.15 and 0.33 with and without snow, respectively. Observed transmittance both with and without snow is contrasted with model results (Figures 6a and 6b) for four different cases: (1) pure sea ice including brine and bubbles; (2) sea ice with brine, bubbles, and measured CDOM absorption; (3) sea ice with brine, bubbles, and particle absorption (but without CDOM); and 4) sea ice with brine, bubbles, CDOM, and particle absorption. Transmittance, absorption, and bottom UV:PAR ratio values from the modeling are listed in supporting information Table S2.

The model run with pure sea ice (Figures 6a and 6b) clearly overestimated light transmission below 550 nm and between 600 and 700 nm, and peak transmittance was shifted from about 560 nm to about 500 nm compared to the observed transmittance. Likewise, the PAR range of the spectrum was overestimated in a run with measured CDOM absorption in addition to pure sea ice. Closest to the observed spectra were the runs that included particle absorption, showing that algae contributed to light attenuation in the ice. Observed PAR transmittance was 6 and 11% lower than modeling with pure sea ice with and without snow, respectively. In terms of fraction of absorbed energy in PAR, pure sea ice with 2 cm snow absorbed 25% less than ice with particles and 2 cm snow (0.03 compared to 0.04).

In the UV range the model runs with measured CDOM and particle absorption spectra gave clearly lower transmittance than observed. Modeling with all constituents resulted in 46 and 36% lower UVA transmittance for snow-covered and bare ice, respectively, than observed; e.g., for snow-covered ice, observed UVA
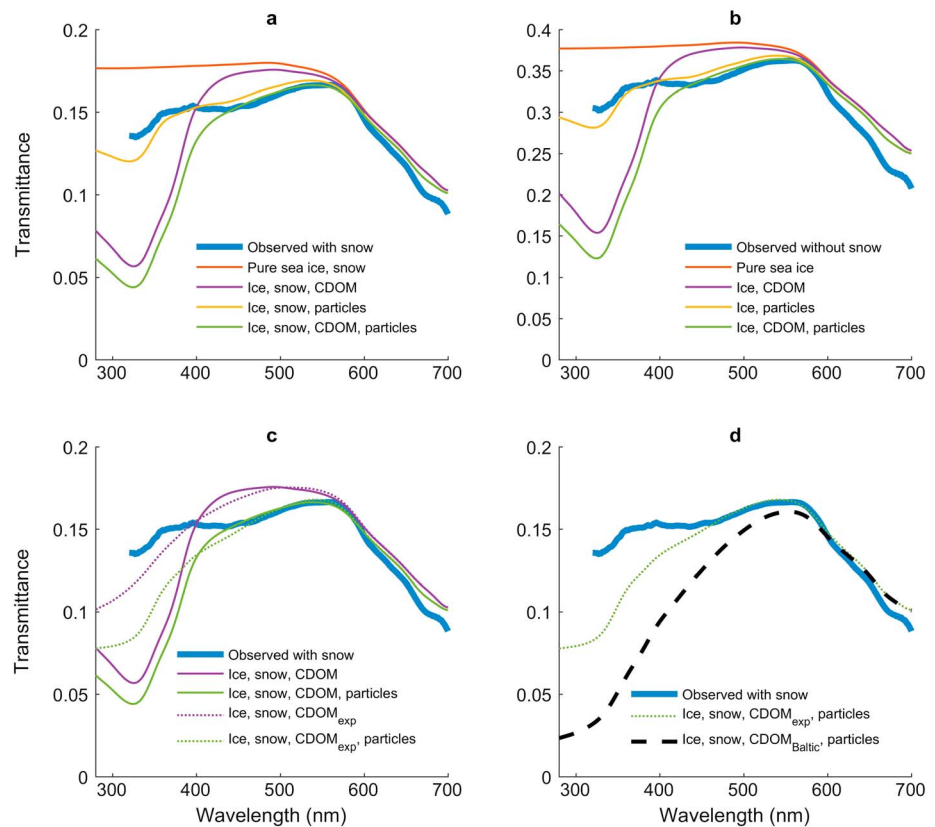
Figure 6. Contribution of the individual components to light transmission at site 3 on 26 May and comparison to Baltic Sea CDOM, examined with the radiative transfer model. Measurements and modeling (a) with snow cover (2 cm) and (b) after snow removal. (c) Modeling with CDOM spectra without MAA peaks (CDOM$_{exp}$). (d) High CDOM case equivalent to Baltic Sea ice [*Uusikivi et al.*, 2010]. Thick blue lines show observed transmittance, and other lines represent model cases with different optical components included (see Table 1 for explanations). "Snow" means the observed 2 cm snow cover. "Pure sea ice" and "ice" include brine and bubbles.

transmittance was 0.15 and modeled (with all constituents) 0.08 (due to the lower limit of the instrument, 320 nm, comparison can only be done for UVA range).

To overcome the model discrepancy in the UV range, an exponential CDOM spectrum, without the MAA peaks, was used in further modeling (see Figure S3). For the part of the spectrum that is affected by MAA absorption (300–425 nm), the spectral slope is calculated based on the values outside the MAA region [*Pavlov et al.*, 2014]. This modification was based on earlier reports of elevated absorption in the UV range after sample handling, caused by leakage of MAAs onto the filter and into the filtrate [*Laurion et al.*, 2003], and will be discussed in section 4.3.

UV transmittance for the exponential (ice and exponential CDOM spectra; without MAA peaks) and measured CDOM case (ice and measured CDOM spectra; with MAA peaks) was, respectively, 0.14 and 0.10 for snow-covered ice (Figure 6c). In other words, using exponential CDOM spectra resulted in 40% higher UV transmittance for snow-covered ice than using the measured spectra. Compared to in situ light measurements, using an exponential CDOM absorption spectrum (together with ice and particle absorption) resulted in 27% lower UVA transmittance for snow-covered ice. Therefore, modeled light attenuation spectrum with the exponential CDOM matched better with that observed but still overestimated attenuation in UV.

The effect of CDOM concentration was investigated by using a CDOM spectrum from Baltic Sea ice ($a_{CDOM} = a_{350} * \exp(-0.0165[\lambda\text{-}350])$, where $a_{350} = 1$ m^{-1}) [*Uusikivi et al.*, 2010], where CDOM concentrations are substantially higher. The observed N-ICE2015 UVA transmittance was 0.15, whereas modeled transmittance with Baltic Sea CDOM (with ice, snow, and particles) was 0.06 (Figure 6d). Compared to the exponential (without MAA peaks) CDOM spectra from N-ICE2015, Baltic Sea-like CDOM absorption resulted in

considerably lower UV transmittance. Compared to the CDOM$_{Baltic}$ case, UV transmittance increased by 0.05 (83%) when modeled with N-ICE2015 exponential CDOM spectra.

For energy accumulation calculations, we took the fraction of absorbed light energy on 26 May as a starting point and multiplied it with the incoming E_d(PAR) (mW m^{-2}) for the following week. The time after 26 May was chosen because the sky was overcast (cloud fraction >0.9) and radiative transfer modeling suggests that in cloudy conditions transmittance varies only very little with solar zenith angle. Biomass in the lead increased on average from 1.3 to 1.4 mg Chl a m^{-2} during the time (until 3 June). Incoming energy in PAR range during the time was 89 MJ m^{-2}. Difference in absorbed light energy in PAR between pure sea ice and ice with particles was 0.03 on 26 May; that is, 3% of incident light energy was absorbed by algae and other particles. If we assume that the fraction of light absorbed by particles remained the same (despite the moderate increase in biomass), particles absorbed 2.7 MJ m^{-2} in a week, or simplified, an algal biomass corresponding to 1.3 mg Chl a absorbed 2.7 MJ in a week. By using density and latent heat for pure ice we can calculate the theoretical maximum of pure ice melting caused by the energy absorbed by particles.

$$dh = \frac{Q}{L \times \rho} \qquad (7)$$

where dh is thickness change, $Q = 2.7$ MJ m^{-2} (absorbed energy), $L = 0.335$ MJ kg^{-1} (latent heat), and $\rho = 918$ kg m^{-3} (ice density). Based on this, the energy absorbed by algae and other particles could have melted 0.8 cm of pure ice in a week, assuming that all absorbed energy ended up as heat.

4. Discussion

4.1. Factors Regulating Light Transmission Through the Refrozen Lead

We assessed the contribution of different properties regulating light transmission through the refrozen lead based on direct irradiance measurements before and after snow removal and radiative transfer modeling to include the effects of particle and CDOM absorption. PAR transmittance T_d(PAR)$_{snow+ice}$ through the refrozen lead was 0.05–0.41 (Figure 2d) which is significantly higher than through the adjacent thicker ice (ice thickness 130 cm with 40 cm of snow, T_d(PAR)$_{snow+ice} < 0.003$) illustrating its role as a window into the underlying ocean. The thick ice measurement site was representative of the study area with an average snow thickness of 43 cm [$Rösel$ et $al.$, 2016]. Snow removal on the refrozen lead further increased PAR transmittance by about twofold to sevenfold (to 0.28–0.49), emphasizing the strong effect by even thin snow cover on PAR transmittance. The variation in transmittance between the lead sites after snow removal could be explained by differences in ice thickness and structure among sites. In particular, the ratio of columnar to granular ice had a strong impact on light transmission, with significantly lower transmittance in ice cores containing thicker granular section. This is consistent with studies showing that light scattering is considerably higher in granular ice than in columnar ice [$Grenfell$ and $Maykut$, 1977; $Uusikivi$ et $al.$, 2010]. This might also explain why T_d(PAR) of the snow-free refrozen lead was considerably lower than the 0.86 measured on snow-free new ice (<15 cm) in Kongsfjorden, Svalbard [$Taskjelle$ et $al.$, 2016b]. The new ice in the study by $Taskjelle$ et $al.$ [2016b] grew in very calm conditions and was thus likely free of granular ice. The variability in granular ice across the refrozen lead cores is likely a result of variable frazil accumulation at the initial stages of ice formation in the lead. Thus, conditions during freezeup, which determine the ice structure, and the amount of granular ice can have a significant impact on thin ice light transmittance.

Calculated K_d(PAR) values (mean 3.7 m^{-1} for ice and mean 43.1 m^{-1} for snow) are within the range of previous studies on thin snow and ice covers. Ehn et $al.$ [2004] report 3.1–4.7 m^{-1} for Baltic Sea ice of similar thickness. Modeling studies by $Hamre$ et $al.$ [2004] showed that K_d for snow on sea ice increases with decreasing snow depth, and resulted in a K_d(PAR) of 88.2 m^{-1} for a 1 cm snow layer. Spectral extinction coefficients for temperate snow by $Perovich$ [2007] were between 20 and 40 m^{-1} for 2–4 cm depth range.

In addition to snow and ice properties, also, the organic constituents in the ice play a significant role in light attenuation and, e.g., protection from UV light [$Perovich$ et $al.$, 1998; $Belzile$ et $al.$, 2000; $Uusikivi$ et $al.$, 2010]. We could not reproduce the observed transmittance without the inclusion of particles in the radiative transfer model. From the organic compounds, particles had higher contribution to PAR transmittance than CDOM: compared to pure sea ice (with snow), ice containing particles had 6% lower transmittance, whereas for

CDOM the effect was not visible (when transmittance is expressed with two-decimal accuracy). Removing snow cover increased transmittance by 120%. To investigate further the role of CDOM (Figure 6d) and algal absorption, additional calculations were made.

CDOM absorption coefficients in the surface water during the lead formation and sampling were generally low (below 0.2 m^{-1} at 350 nm) [*Pavlov et al.*, 2017b]. Therefore, absorption by CDOM in sea ice formed in these surface waters is relatively low as well and likely does not represent a significant factor of UV protection for organisms in the same way it does in waters with high CDOM concentration found in other Arctic locations influenced by terrigenous CDOM [*Granskog et al.*, 2012; *Pavlov et al.*, 2015]. In this regard, ice in the refrozen lead presented here is different from, e.g., the Baltic Sea, where similar studies were made on thin ice [*Uusikivi et al.*, 2010; *Piiparinen et al.*, 2015]. We show how CDOM at high concentration, like measured from Baltic Sea ice, has a larger contribution to total light attenuation than the lead ice CDOM and high concentrations of MAAs in the ice algae combined (Figure 6d). The reduced UV transmittance caused by high CDOM absorption in the Baltic Sea ice is a possible reason for large differences in total MAA concentration (see discussion in section 4.2) between the lead and the Baltic Sea studies. Ice algae living in low CDOM areas have to invest considerably more in UV protection.

The potential effect of algal absorption on ice melt was estimated. During the last week of sampling, energy absorption by particles could theoretically melt almost 1 cm sea ice. While this is a rough estimate and does not take into account ice thermodynamics or, e.g., the distribution of algae in the ice [*Zeebe et al.*, 1996], it demonstrates that even with low biomass, but under high irradiance, ice algae have the potential to affect ice growth and thickness in scales relevant for the ice algal habitat. In a modeling study, *Zeebe et al.* [1996] were operating with considerably higher ice algal standing stocks than in our study, but the ice was much thicker (>1.6 m), strongly limiting the available irradiance at the algal layer. Thickness of melted ice in the study by *Zeebe et al.* [1996] was on the order of centimeters over the course of the melting period (40 days). Further studies could conclude if this mechanism limits biomass buildup in thin ice covers, by causing melt-out when ice-algal biomass reaches a certain level.

4.2. MAA Production

The MAA concentrations in the lead ice were occasionally very high (up to 39 mg m^{-3} for individual samples), and the bulk MAA:Chl *a* ratios are, to our knowledge, the highest ever reported for sea ice (up to 6.3 mg MAA m^{-3} per mg Chl *a* m^{-3} for individual samples). The highest total MAA concentrations were recorded in the ice bottom on 20 and 26 May (Figure 4b), when increased Chl *a* concentration was also seen compared to the preceding days. Because of the lack of standards for all encountered MAA compounds, total MAA concentration in the cells was higher than what was measured, and our results are thus a conservative estimate of the MAA concentration. Total concentrations in Baltic Sea ice have been reported to be <2 mg m^{-3} [*Uusikivi et al.*, 2010] and <3.5 mg m^{-3} [*Piiparinen et al.*, 2015]. *Elliott et al.* [2015] reported relative concentrations (Canadian Arctic Archipelago) but estimated maximum concentrations of 21.9 and 19.9 mg m^{-3} for shinorine and porphyra-334, respectively (total concentration per sample not specified). When it comes to the bulk MAA:Chl *a* ratio, *Ryan et al.* [2002] refer mean ratios below 0.03 (volumetric concentrations not given), *Uusikivi et al.* [2010] and *Piiparinen et al.* [2015] obtained ratios below 1 (highest ratios at ice surface), and *Elliott et al.* [2015] up to 0.6 (based on the estimated total MAA concentration).

The most apparent explanation for the high MAA production in our case is the high light environment under thin snow and ice cover. MAAs can have many roles in a cell [*Oren and Gunde-Cimerman*, 2007], but the major function of MAAs in marine algae seems to be functioning as UV protection and antioxidants [*Carreto et al.*, 2011]. *Helbling et al.* [1996] observed clear reduction of algal photoinhibition when MAAs were present. Naturally, MAAs can simultaneously serve several purposes. Sea ice is a challenging environment regarding osmotic balance, but the very high MAA concentrations found in our study (e.g., 20 May) are unlikely a response to osmotic stress because brine salinities in the lead ice (32.9–45.0 on 20 May) were not exceptionally high and close to seawater salinity. In addition, bulk salinity decreased, whereas MAA concentration in general increased over the sampling period (Figure 2).

4.3. Absorption Patterns

Generally, particle and algal absorption increased during the sampling period, following the increase in ice algal biomass (Figures 2e, 3c, 3e, 5a, and 5b). Days with high biomass or detrital content did not strictly

follow the temporal trend. Chl *a*-specific absorption decreased during the period (Figures 3f, 5c, and 5d). Average specific absorption efficiency ("packaging effect," the ratio of Chl *a*-specific absorption at 674 nm to the theoretical maximum at this wavelength), calculated as in *Johnsen and Sakshaug* [2007], decreased from 0.64 to 0.28 over the study period. A higher value indicates lower packaging [*Johnsen and Sakshaug*, 2007] which can be attributed to small cell sizes or to low pigment content due to high-light acclimation [*Kirk*, 2011]. Because the algae likely acclimated from low light to high light over the study period (see discussion in section 4.5), the increasing packaging could possibly be explained by species succession in the lead ice and subsequent increase in cell size. Flagellates and small centric diatoms colonized the lead ice in the beginning [*Olsen et al.*, 2017]. Toward the end of the sampling period, the pennate diatoms *Nitzschia frigida* and *Navicula* spp., characteristic of ice bottom assemblages [*Leu et al.*, 2015], became dominant [*Olsen et al.*, 2017]. These findings highlight the complex relationship between absorption coefficients and pigment packaging in natural samples by showing that pigment packaging in this young ice environment was likely controlled by both light and species composition.

Distinct absorption peaks in the UV range were observed in both CDOM and particle absorption samples (Figures 3c, 3e–3g, and 5), likely caused by MAAs. However, the magnitude of the peaks has to be treated with caution. As *Laurion et al.* [2003] points out, MAAs can be released from cells, in this case dinoflagellates, during sampling procedures like thawing of frozen filters, which results in unpacked (exaggerated) absorption of the compounds spread on the filter. In sections 3 and 4 we therefore only concentrate on the location of the absorption peaks as we consider that aspect as uncompromised data. However, the MAA peaks in our particle absorption spectra are more in line with the peaks in the visible part, compared to the disproportionally high MAA peaks (up to almost 9 times higher than the blue peak at 440 nm) obtained in the above mentioned experiments by *Laurion et al.* [2003]. Likewise, CDOM absorption might be affected by sample handling. A field experiment we conducted in 2016 indicates that the ice core melting method affected the measured UV absorption in CDOM samples. MAA peaks (at 330 nm and 360 nm) were visible only in CDOM absorption spectra from samples melted directly (without addition of filtered seawater). In this study direct melting was used and thus CDOM spectra can be affected by the damage caused in the algal cells due to osmotic shock [*Miller et al.*, 2015]. Further, improvement in the model and observation agreement obtained by the removal of MAA peaks (Figure 6c) indicates that CDOM absorption coefficients in the MAA range were overestimated. This potential effect should be taken into consideration, and all sea ice studies should report the melting method to be able to assess possible artifacts. However, for CDOM samples buffered melting would not be straightforward because adding filtered seawater to the ice sample also introduces random CDOM from the water column. Melting with artificial seawater free of organics could possibly be an option, but further experiments are needed. Release of MAAs probably varies between algal species, some being more robust to handling (e.g., diatoms with hard silica frustules), and more studies are also needed to understand the consequences of other sampling procedures like filtration method.

4.4. Linking Algal Absorption Characteristics and Different MAA Compounds

The primary MAA peak in the particle absorption spectra is around 330 nm, where many different MAAs absorb, including the compounds we had standards for, shinorine (absorption maximum at 333 nm), palythine (320 nm), and porphyra-334 (334 nm) [*Carreto et al.*, 2011], and the fourth, unknown compound present in the samples (331 nm). The fifth, unknown compound ("U2") present in our samples, possibly a condensation product of euhalothece-362 and another MAA [*Elliott et al.*, 2015], had an absorption maximum at 363 nm. This fits well with particle absorption characteristics on two sampling days (20 and 29 May, secondary peak around 365 nm) and the presence of U2 compound (mainly 20 and 29 May). However, the second MAA peak in CDOM samples at around 360 nm (Figures 5e and 5f) was present in most samples (most notable in ice core tops samples). In particle absorption spectra, a second peak around 380 nm is visible especially in many ice core top samples (Figures 5b and 5d). All MAA components reported in literature have absorption peaks <362 nm [*Karentz*, 2001; *Carreto et al.*, 2011]. This second peak could be attributed to a UV-absorbing compound that is not a MAA and thus was not detected with the method used. The compound could also be responsible for the 360 nm peak in the CDOM absorption spectra, because of possibly different absorption characteristics for in vivo and in vitro, which is well known for chlorophylls and carotenoids, due to binding to different proteins when intact in cells [*Kirk*, 2011]. This unidentified compound becomes more important toward the end of the sampling, seen as increased absorption (Figure 4d). Also, its stronger role in the ice core

tops seems to indicate that it is produced in response to high light exposure. Likewise, the presence of the unknown U2 compound in our samples, as well as shinorine being abundant, agree with earlier studies [*Elliott et al.*, 2015] that connect these compounds with high light exposure.

4.5. Biomass Buildup in Young Ice

The ice algal standing stock in the lead ice was 0.06–2.31 mg Chl a m^{-2}. This is similar to previous estimates of ice algal standing stocks (summarized by *Leu et al.* [2015]) in the Atlantic sector of the Arctic during spring (March to May): 0.1–5.5 mg Chl a m^{-2} in Fram Strait and Greenland Sea pack ice, and 0.3–9.8 mg m^{-2} in pack ice around Svalbard. In areas affected by warm Atlantic water inflow, bottom ice ablation, which deteriorates the ice algal habitat, is suggested to be the limiting factor for ice algal biomass buildup [*Leu et al.*, 2015].

Interestingly, ice algal standing stock in the newly formed ice was similar to those of the surrounding thicker and older ice during the study time. The second-year ice (122–145 cm thick with 38–56 cm snow cover) contained 1.1–2.4 mg Chl a m^{-2} [*Olsen et al.*, 2017]. Thus, the algae in the newly formed ice reached comparable standing stocks to that of the surrounding older ice, despite thicker ice column and larger seeding stock of algae in the latter. However, considering the very low irradiance under the thick ice (1–2 μmol photons m^{-2} s^{-1} [*Olsen et al.*, 2017; *Taskjelle et al.*, 2016a], compared to 30–350 μmol photons m^{-2} s^{-1} in the lead), the thin ice environment was expected to be more productive.

Olsen et al. [2017] suggest that the refrozen lead was seeded by sea ice algae (specifically the dominant pennate diatom *Nitzschia frigida*) from the adjacent thick ice. The photoacclimation process from a low light environment (thick ice) to a high light environment (newly formed refrozen lead ice) might be similar to the one observed by *Juhl and Krembs* [2010]. They found that algal biomass response to snow removal was, in addition to physical processes, dependent on initial snow depth (i.e., light environment and therefore light acclimation status of algae). From laboratory experiments they concluded that photoacclimation of *Nitzschia frigida* from 1–2 to 110 μmol photons m^{-2} s^{-1} took between 3 and 6 days. In nonacclimated cells, growth rate decreased following transfer to high light intensities, but for high-light-acclimated cells no growth inhibition could be observed (at irradiances up to 110 μmol photons m^{-2} s^{-1}) [*Juhl and Krembs*, 2010]. Therefore, we hypothesize that the initial algal community of the refrozen lead might have undergone a similar photoacclimation process delaying its growth and resulting in the lower than expected algal biomass.

Over time, ice algae in the refrozen lead seem to become high-light acclimated. On 26 May, the optimal irradiance at which maximum photosynthetic rates occurred was 210–330 μmol photons m^{-2} s^{-1} and E_k (photoacclimation parameter) was 110–200 μmol photons m^{-2} s^{-1}, based on photosynthesis vs irradiance curves (M. Fernández-Méndez, unpublished data, 2015). Photoinhibition occurred above 250 to 350 μmol photons m^{-2} s^{-1}. Based on the in situ measurements, undertaken between 12 and 14 local time on the sampling days, highest E_d(PAR) average (average of five sites) was 240 μmol photons m^{-2} s^{-1}. Thus, irradiance was likely below photoinhibiting levels during the latter part of the study, but based on literature, the irradiance levels could cause photoinhibition for unacclimated cells [*Kühl et al.*, 2001; *Juhl and Krembs*, 2010]. This is supported by the fact that biomass was high on 20 May, when snow cover was the thickest and thus transmittance was among the lowest (Figure 2). Increasing biomass toward the end of the sampling despite increasing irradiance could be explained by the photoacclimation that had occurred by that time.

The high MAA production indicates the need for active photoprotection against damaging UV radiation levels and is possibly associated with a high metabolic cost, which could further explain the lower than expected biomass accumulation in the thin ice. *Hernando et al.*, [2002, 2011] observed lower cell numbers and higher MAA production in Antarctic diatom (*Thalassiosira* sp.) cultures that received higher UV exposure and suggested that growth was compromised by photoprotective compound synthesis. Initial growth inhibition in diatoms following elevated UV exposure was reported also by, e.g., *Zudaire and Roy* [2001]. However, MAA synthesis was not maintained over the whole experiment but replaced by elevated diatoxanthin levels, maybe because of the energetic costs of the MAA synthesis. This could be similar to our observations, where Chl a to MAA ratios declined toward the end of the study period. In the ice core tops, however, the ratios remained still high. According to *Shick and Dunlap* [2002] evidence on metabolic costs and growth effect of MAA production is inconclusive, but the cost of producing MAAs is estimated to be similar to Chl a synthesis. Considering the very high ratios of MAAs to Chl a in our samples, it seems likely that MAA production affected the growth rates negatively.

Phytoplankton growth clearly benefitted from the higher light transmittance through thin ice and open leads, resulting in an under-ice bloom with Chl a standing stocks (integrated for the upper 50 m) of up to 233 mg Chl a m^{-2} [*Assmy et al.*, 2017a]. Unlike the ice algae, phytoplankton is being vertically mixed through the water column, reducing the probability of photoinhibition and increasing nutrient replenishment. Silicate limitation was possibly one important factor restricting growth in the thin ice, as indicated by biogeochemical modeling [*Duarte et al.*, 2017]. Furthermore, in this particular case the water column bloom was dominated by *Phaeocystis pouchetii* which is a very plastic species with regard to photoacclimation, suggesting that it can acclimate to the alternating light field provided by the heterogenous ice cover [*Assmy et al.*, 2017a]. Further studies could show how the thin ice algal community evolves after the initial period described here—the lead ice broke up on June 4—but based on our observations, the leads in the area enhanced mainly the phytoplankton production.

5. Conclusions

Here we present unique bio-optical observations and PAR transmittance of newly formed Arctic sea ice in a lead in spring. While the dominating thicker ice with thicker snow cover transmitted very little E_d(PAR) (<0.3%) to the bottom ice algal community and the underlying water column, leads act like windows into the water column with 5–40% transmittance in this study. We showed how even a thin snow cover and the conditions during refreezing of leads, affecting ice structure, are important for how effective these windows are in transmitting light. The water masses in the area and the lead ice were low in CDOM concentration, requiring the need for UV protection compounds (MAAs), which the algae synthetized in high concentrations.

Our results indicate that growth of shade-acclimated ice algae in newly formed thin ice may be compromised by the need for photoacclimation to a high light environment and investment in photoprotective pigments. In addition, ice bottom melt caused by algal absorption even at relatively low biomass has the potential to limit ice algal biomass accumulation in thin ice environments. Indeed, the growth of a large under-ice bloom supported by the added sunlight through open and refrozen leads indicates that phytoplankton rather than ice algae profited from an ice cover with frequent leads. The occurrence of leads may become more common in the future Arctic as the dynamics of the ice pack increases, which could have a profound impact on the sea ice-associated ecosystem.

References

Arrigo, K. R., and G. L. van Dijken (2015), Continued increases in Arctic Ocean primary production, *Prog. Oceanogr.*, *136*, 60–70, doi:10.1016/j.pocean.2015.05.002.

Assmy, P., et al. (2017a), Leads in Arctic pack ice enable early phytoplankton blooms below snow-covered sea ice, *Sci. Rep.*, *7*, 40850, doi:10.1038/srep40850.

Assmy, P., et al. (2017b), N-ICE2015 sea ice biogeochemistry, Norwegian Polar Institute, doi:10.21334/npolar.2017.d3e93b31.

Belzile, C., S. C. Johannessen, M. Gosselin, S. Demers, and W. L. Miller (2000), Ultraviolet attenuation by dissolved and particulate constituents of first-year ice during late spring in an Arctic polynya, *Limnol. Oceanogr.*, *45*(6), 1265–1273, doi:10.4319/lo.2000.45.6.1265.

Brunet, C., G. Johnsen, J. Lavaud, and S. Roy (2011), Pigments and photoacclimation processes, in *Phytoplankton Pigments—Characterization, Chemotaxonomy and Applications in Oceanography*, edited by S. Roy et al., pp. 445–471, Cambridge Univ. Press, Cambridge.

Campbell, K., C. J. Mundy, D. G. Barber, and M. Gosselin (2014), Remote estimates of ice algae biomass and their response to environmental conditions during spring melt, *Arctic*, *67*(3), 375–387, doi:10.14430/arctic4409.

Campbell, K., C. J. Mundy, D. G. Barber, and M. Gosselin (2015), Characterizing the sea ice algae chlorophyll *a*-snow depth relationship over Arctic spring melt using transmitted irradiance, *J. Mar. Syst.*, *147*, 76–84, doi:10.1016/j.jmarsys.2014.01.008.

Carignan, M. O., and J. I. Carreto (2013), Characterization of mycosporine-serine-glycine methyl ester, a major mycosporine-like amino acid from dinoflagellates: A mass spectrometry study, *J. Phycol.*, *49*(4), 680–688, doi:10.1111/jpy.12076.

Carreto, J. I., M. O. Carignan, and N. G. Montoya (2005), A high-resolution reverse-phase liquid chromatography method for the analysis of mycosporine-like amino acids (MAAs) in marine organisms, *Mar. Biol.*, *146*(2), 237–252, doi:10.1007/s00227-004-1447-y.

Carreto, J. I., S. Roy, K. Whitehead, C. A. LLewellyn, and M. O. Carignan (2011), UV-absorbing "pigments": Mycosporine-like amino acids, in *Phytoplankton Pigments—Characterization, Chemotaxonomy and Applications in Oceanography*, edited by S. Roy, C. A. Llewellyn, and E. S. Egeland, pp. 412–441, Cambridge Univ. Press, Cambridge.

Cohen, L., S. R. Hudson, V. P. Walden, R. M. Graham, and M. A. Granskog (2017), Meteorological conditions in a thinner Arctic sea ice regime from winter through summer during the Norwegian Young Sea ICE expedition (N-ICE2015), *J. Geophys. Res. Atmos.*, doi:10.1002/2016JD026034.

Conde, F. R., M. S. Churio, and C. M. Previtali (2000), The photoprotector mechanism of mycosporine-like amino acids. Excited-state properties and photostability of porphyra-334 in aqueous solution, *J. Photochem. Photobiol. B Biol.*, *56*(2–3), 139–144, doi:10.1016/S1011-1344(00)00066-X.

Cox, G. F. N., and W. F. Weeks (1986), Changes in the salinity and porosity of sea-ice samples during shipping and storage, *J. Glaciol.*, *32*(112), 371–375.

Duarte, P., et al. (2017), Sea ice thermodynamics and biogeochemistry in the Arctic Ocean: Empirical and model results, *J. Geophys. Res. Biogeosci.*, *122*, doi:10.1002/2016JG003660.

Ehn, J., M. A. Granskog, A. Reinart, and A. Erm (2004), Optical properties of melting landfast sea ice and underlying seawater in Santala Bay, Gulf of Finland, *J. Geophys. Res., 109*, C09003, doi:10.1029/2003JC002042.

Elliott, A., C. J. Mundy, M. Gosselin, M. Poulin, K. Campbell, and F. Wang (2015), Spring production of mycosporine-like amino acids and other UV-absorbing compounds in sea ice associated algae communities in the Canadian Arctic, *Mar. Ecol. Prog. Ser., 541*, 91–104, doi:10.3354/meps11540.

Fountoulakis, I., A. F. Bais, K. Tourpali, K. Fragkos, and S. Misios (2014), Projected changes in solar UV radiation in the Arctic and sub-Arctic oceans: Effects from changes in reflectivity, ice transmittance, clouds, and ozone, *J. Geophys. Res. Atmos., 119*, 8073–8090, doi:10.1002/2014JD021918.

Fritsen, C. H., E. D. Wirthlin, D. K. Momberg, M. J. Lewis, and S. F. Ackley (2011), Bio-optical properties of Antarctic pack ice in the early austral spring, *Deep Sea Res., Part II, 58*(9–10), 1052–1061, doi:10.1016/j.dsr2.2010.10.028.

Gerland, S., M. A. Granskog, J. A. King, and A. Rösel (2017), N-ICE2015 ice core physics: Temperature, salinity and density [data set], Norwegian Polar Institute, doi:10.21334/npolar.2017.c3db82e3.

Granskog, M. A., C. A. Stedmon, P. A. Dodd, R. M. W. Amon, A. K. Pavlov, L. De Steur, and E. Hansen (2012), Characteristics of colored dissolved organic matter (CDOM) in the Arctic outflow in the Fram Strait: Assessing the changes and fate of terrigenous CDOM in the Arctic Ocean, *J. Geophys. Res., 117*, C12021, doi:10.1029/2012JC008075.

Granskog, M. A., P. Assmy, S. Gerland, G. Spreen, H. Steen, and L. H. Smedsrud (2016), Arctic research on thin ice: Consequences of Arctic sea ice loss, *Eos. Trans. AGU, 97*(5), 22–26.

Grenfell, T. C., and G. A. Maykut (1977), The optical properties of ice and snow in the Arctic basin, *J. Glaciol., 18*(80), 445–463.

Hamre, B., J. G. Winther, S. Gerland, J. J. Stamnes, and K. Stamnes (2004), Modeled and measured optical transmittance of snow-covered first-year sea ice in Kongsfjorden, Svalbard, *J. Geophys. Res., 109*, C10006(C10006), doi:10.1029/2003JC001926.

Hamre, B., S. Stamnes, K. Stamnes, and J. Stamnes (2017), AccuRT: A versatile tool for radiative transfer simulations in the coupled atmosphere-ocean system, *AIP Conf. Proc., 1810*(1), 120002, doi:10.1063/1.4975576.

Helbling, E. W., B. E. Chalker, W. C. Dunlap, O. Holm-Hansen, and V. E. Villafañe (1996), Photoacclimation of antarctic marine diatoms to solar ultraviolet radiation, *J. Exp. Mar. Biol. Ecol., 204*(96), 85–101.

Hernando, M., J. I. Carreto, M. O. Carignan, G. A. Ferreyra, and C. Gross (2002), Effects of solar radiation on growth and mycosporine-like amino acids content in *Thalassiosira* sp., an Antarctic diatom, *Polar Biol., 25*, 12–20, doi:10.1007/s003000100306.

Hernando, M. P., J. I. Carreto, M. Carignan, and G. A. Ferreyra (2011), Effect of vertical mixing on short-term mycosporine-like amino acid synthesis in the Antarctic diatom, *Thalasiossira* sp, *Sci. Mar., 76*(1), 49–57, doi:10.3989/scimar.03203.16D.

Holm-Hansen, O., and B. Riemann (1978), Chlorophyll *a* determination: Improvements in methodology, *Oikos, 30*(3), 438–447.

Hudson, S. R., and L. Cohen (2015), N-ICE2015 surface meteorology v2 [data set], Norwegian Polar Institute, doi:10.21334/npolar.2015.056a61d1.

Itkin, P., G. Spreen, B. Cheng, M. Doble, F. Girard-Ardhuin, J. Haapala, N. Hughes, L. Kaleschke, M. Nicolaus, and J. Wilkinson (2017), Thin ice and storms: A case study of sea ice deformation from buoy arrays deployed during N-ICE2015, *J. Geophys. Res. Oceans*, doi:10.1002/2016JC012403.

Johnsen, G., and E. Sakshaug (2007), Biooptical characteristics of PSII and PSI in 33 species (13 pigment groups) of marine phytoplankton, and the relevance for pulse-amplitude-modulated and fast-repetition-rate fluorometry, *J. Phycol., 43*(6), 1236–1251, doi:10.1111/j.1529-8817.2007.00422.x.

Juhl, A. R., and C. Krembs (2010), Effects of snow removal and algal photoacclimation on growth and export of ice algae, *Polar Biol., 33*(8), 1057–1065, doi:10.1007/s00300-010-0784-1.

Karentz, D. (1994), Ultraviolet tolerance mechanisms in Antarctic marine organisms, in *Ultraviolet Radiation in Antarctica: Measurements and Biological Effects. Antarctic Research Series*, edited by C. S. Weiler and P. A. Penhale, pp. 93–110, AGU, Washington, D. C.

Karentz, D. (2001), Chemical defenses of marine organisms against solar radiation exposure: UV-absorbing mycosporine-like amino acids and scytonemin, in *Marine Chemical Ecology*, edited by J. McClintock and W. Baker, pp. 481–520, CRC Press, Boca Raton, Fla.

Kauko, H. M., A. K. Pavlov, E. Nystedt, and M. A. Granskog (2017), N-ICE2015 particulate matter absorption spectra, Norwegian Polar Institute, doi:10.21334/npolar.2017.35978199.

Kirk, J. T. O. (2011), *Light and Photosynthesis in Aquatic Ecosystems*, 3d ed., pp. 292 & 311–319, Cambridge Univ. Press, Cambridge.

Kwok, R., G. Spreen, and S. Pang (2013), Arctic sea ice circulation and drift speed: Decadal trends and ocean currents, *J. Geophys. Res. Oceans, 118*, 2408–2425, doi:10.1002/jgrc.20191.

Kühl, M., R. N. Glud, J. Borum, R. Roberts, and S. Rysgaard (2001), Photosynthetic performance of surface-associated algae below sea ice as measured with a pulse-amplitude-modulated (PAM) fluorometer and O$_2$ microsensors, *Mar. Ecol. Prog. Ser., 223*(1), 1–14, doi:10.3354/meps223001.

Lange, M. A. (1988), Basic properties of Antarctic sea ice as revealed by textural analysis of ice cores, *Ann. Glaciol., 10*, 95–101.

Laurion, I., F. Blouin, and S. Roy (2003), The quantitative filter technique for measuring phytoplankton absorption: Interference by MAAs in the UV waveband, *Limnol. Oceanogr. Methods, 1*, 1–9, doi:10.4319/lom.2011.1.1.

Leppäranta, M., and T. Manninen (1988), The brine and gas content of sea ice with attention to low salinities and high temperatures, *Finnish Inst. Mar. Res. Intern. Rep., 2*, 1–14.

Leu, E., C. J. Mundy, P. Assmy, K. Campbell, T. M. Gabrielsen, M. Gosselin, T. Juul-Pedersen, and R. Gradinger (2015), Arctic spring awakening—Steering principles behind the phenology of vernal ice algal blooms, *Prog. Oceanogr., 139*, 151–170, doi:10.1016/j.pocean.2015.07.012.

Logvinova, C. L., K. E. Frey, and L. W. Cooper (2016), The potential role of sea ice melt in the distribution of chromophoric dissolved organic matter in the Chukchi and Beaufort seas, *Deep Sea Res., II, 130*, 28–42, doi:10.1016/j.dsr2.2016.04.017.

Mason, J. D., M. T. Cone, and E. S. Fry (2016), Ultraviolet (250–550 nm) absorption spectrum of pure water, *Appl. Opt., 55*(25), 7163–7172, doi:10.1364/AO.55.007163.

McDougall, T. J., D. R. Jackett, F. J. Millero, R. Pawlowicz, and P. M. Barker (2012), A global algorithm for estimating Absolute Salinity, *Ocean Sci., 8*(6), 1123–1134, doi:10.5194/os-8-1123-2012.

Meier, W. N., et al. (2014), Arctic sea ice in transformation: A review of recent observed changes and impacts on biology and human activity, *Rev. Geophys., 51*, 185–217, doi:10.1002/2013RG000431.

Meyer, A., et al. (2017), Winter to summer oceanographic observations in the Arctic Ocean north of Svalbard, *J. Geophys. Res. Oceans*, doi:10.1002/2016JC012391.

Miller, L. A., et al. (2015), Methods for biogeochemical studies of sea ice: The state of the art, caveats, and recommendations, *Elem. Sci. Anthr., 3*, 38, doi:10.12952/journal.elementa.000038.

Mueller, J. L., G. S. Fargion, C. R. McClain, S. Pegau, J. R. V. Zanefeld, B. G. Mitchell, M. Kahru, J. Wieland, and M. Stramska (2003), Ocean optics protocols for satellite ocean color sensor validation, revision 4, volume IV: Inherent optical properties: Instruments, characterizations, field measurements and data analysis protocols, NASA Tech. Rep., NASA Goddard Space Flight Center, Greenbelt, Md.

Mundy, C. J., D. G. Barber, and C. Michel (2005), Variability of snow and ice thermal, physical and optical properties pertinent to sea ice algae biomass during spring, *J. Mar. Syst.*, *58*, 107–120, doi:10.1016/j.jmarsys.2005.07.003.

Mundy, C. J., et al. (2011), Characteristics of two distinct high-light acclimated algal communities during advanced stages of sea ice melt, *Polar Biol.*, *34*(12), 1869–1886, doi:10.1007/s00300-011-0998-x.

Nicolaus, M., C. Katlein, J. Maslanik, and S. Hendricks (2012), Changes in Arctic sea ice result in increasing light transmittance and absorption, *Geophys. Res. Lett.*, *39*, L24501, doi:10.1029/2012GL053738.

Olsen, L. M., et al. (2017), The seeding of ice algal blooms in Arctic pack ice: The multiyear ice seed repository hypothesis, *J. Geophys. Res. Biogeosci.*, *122*, doi:10.1002/2016JG003668.

Oren, A., and N. Gunde-Cimerman (2007), Mycosporines and mycosporine-like amino acids: UV protectants or multipurpose secondary metabolites?, *FEMS Microbiol. Lett.*, *269*(1), 1–10, doi:10.1111/j.1574-6968.2007.00650.x.

Pavlov, A. K., A. Silyakova, M. A. Granskog, R. G. J. Bellerby, A. Engel, K. G. Schulz, and C. P. D. Brussaard (2014), Marine CDOM accumulation during a coastal Arctic mesocosm experiment: No response to elevated pCO_2, *J. Geophys. Res. Biogeosci.*, *119*, 1216–1230, doi:10.1002/2013JG002587.

Pavlov, A. K., M. A. Granskog, C. A. Stedmon, B. V. Ivanov, S. R. Hudson, and S. Falk-Petersen (2015), Contrasting optical properties of surface waters across the Fram Strait and its potential biological implications, *J. Mar. Syst.*, *143*, 62–72, doi:10.1016/j.jmarsys.2014.11.001.

Pavlov, A. K., H. M. Kauko, C. Stedmon, and M. A. Granskog (2017a), N-ICE2015 colored dissolved organic matter absorption spectra, Norwegian Polar Institute, doi:10.21334/npolar.2017.f46970ba.

Pavlov, A. K., T. Taskjelle, B. Hamre, H. M. Kauko, S. R. Hudson, P. Assmy, P. Duarte, M. Fernández Méndez, C. J. Mundy, and M. A. Granskog (2017b), Altered inherent optical properties and estimates of the underwater light field during an Arctic under-ice bloom of *Phaeocystis pouchetii*, *J. Geophys. Res. Oceans*, *122*, doi:10.1002/2016JC012471.

Perovich, D. K. (1990), Theoretical estimates of light reflection and transmission by spatially complex and temporally varying sea ice covers, *J. Geophys. Res.*, *95*(C6), 9557–9567, doi:10.1029/JC095iC06p09557.

Perovich, D. K. (2007), Light reflection and transmission by a temperate snow cover, *J. Glaciol.*, *53*(181), 201–210, doi:10.3189/172756507782202919.

Perovich, D. K., C. S. Roesler, and W. S. Pegau (1998), Variability in Arctic sea ice optical properties, *J. Geophys. Res.*, *103*, 1193–1208, doi:10.1029/97JC01614.

Petrich, C., M. Nicolaus, and R. Gradinger (2012), Sensitivity of the light field under sea ice to spatially inhomogeneous optical properties and incident light assessed with three-dimensional Monte Carlo radiative transfer simulations, *Cold Reg. Sci. Technol.*, *73*, 1–11, doi:10.1016/j.coldregions.2011.12.004.

Piiparinen, J., S. Enberg, J.-M. Rintala, R. Sommaruga, M. Majaneva, R. Autio, and A. Vähätalo (2015), The contribution of mycosporine-like amino acids, chromophoric dissolved organic matter and particles to the UV protection of sea-ice organisms in the Baltic Sea, *Photochem. Photobiol. Sci.*, doi:10.1039/C4PP00342J.

Pope, R. M., and E. S. Fry (1997), Absorption spectrum (380–700 nm) of pure water. II. Integrating cavity measurements, *Appl. Opt.*, *36*(33), 8710–8723.

Rintala, J.-M., J. Piiparinen, J. Blomster, M. Majaneva, S. Müller, J. Uusikivi, and R. Autio (2014), Fast direct melting of brackish sea-ice samples results in biologically more accurate results than slow buffered melting, *Polar Biol.*, *37*(12), 1811–1822, doi:10.1007/s00300-014-1563-1.

Ryan, K. G., A. McMinn, K. A. Mitchel, and L. Trenerry (2002), Mycosporine-like amino acids in Antarctic sea ice algae, and their response to UVB radiation, *Z. Naturforsch.*, *57c*, 471–477.

Rösel, A., et al. (2016), N-ICE2015 snow depth data with Magnaprobe, Norwegian Polar Institute, doi:10.21334/npolar.2016.3d72756d.

Shick, J. M., and W. C. Dunlap (2002), Mycosporine-like amino acids and related gadusols: Biosynthesis, accumulation, and UV-protective functions in aquatic organisms, *Annu. Rev. Physiol.*, *64*(1), 223–262, doi:10.1146/annurev.physiol.64.081501.155802.

Stamnes, K., B. Hamre, J. J. Stamnes, G. Ryzhikov, M. Biryulina, R. Mahoney, B. Hauss, and A. Sei (2011), Modeling of radiation transport in coupled atmosphere-snow-ice-ocean systems, *J. Quant. Spectrosc. Radiat. Transf.*, *112*(4), 714–726, doi:10.1016/j.jqsrt.2010.06.006.

Stedmon, C. A., S. Markager, and H. Kaas (2000), Optical properties and signatures of chromophoric dissolved organic matter (CDOM) in Danish coastal waters, *Estuar. Coast. Shelf Sci.*, *51*(2), 267–278, doi:10.1006/ecss.2000.0645.

Steiner, N., C. Deal, D. Lannuzel, D. Lavoie, F. Massonnet, L. A. Miller, S. Moreau, E. Popova, J. Stefels, and L. Tedesco (2016), What sea-ice biogeochemical modellers need from observers, *Elem. Sci. Anthr.*, *4*, 84, doi:10.12952/journal.elementa.000084.

Taskjelle, T., S. R. Hudson, A. K. Pavlov, and M. A. Granskog (2016a), N-ICE2015 surface and under-ice spectral shortwave radiation data [data set], Norwegian Polar Institute, doi:10.21334/npolar.2016.9089792e.

Taskjelle, T., S. R. Hudson, M. A. Granskog, M. Nicolaus, R. Lei, S. Gerland, J. J. Stamnes, and B. Hamre (2016b), Spectral albedo and transmittance of thin young Arctic sea ice, *J. Geophys. Res. Oceans*, *121*, 540–553, doi:10.1002/2015JC011254.

Taskjelle, T., M. A. Granskog, A. K. Pavlov, S. R. Hudson, and B. Hamre (2017), Effects of an Arctic under-ice bloom on solar radiant heating of the water column, *J. Geophys. Res. Oceans*, *122*, 126–138, doi:10.1002/2016JC012187.

Tassan, S., and G. M. Ferrari (2002), A sensitivity analysis of the "transmittance–reflectance" method for measuring light absorption by aquatic particles, *J. Plankton Res.*, *24*(8), 757–774.

Thomas, G. E., and K. Stamnes (1999), *Radiative Transfer in the Atmosphere and Ocean*, 548 pp., Cambridge Univ. Press, Cambridge.

Tilstone, G. H., G. F. Moore, K. Sørensen, R. Doerffer, R. Røttgers, K. G. Ruddick, R. Pasterkamp, and P. V Jørgensen (2002), Regional validation of MERIS chlorophyll products in North Sea coastal waters, REVAMP methodologies – EVG1 – CT – 2001 - 00049.

Uusikivi, J., A. Vähätalo, M. A. Granskog, and R. Sommaruga (2010), Contribution of mycosporine-like amino acids and colored dissolved and particulate matter to sea ice optical properties and ultraviolet attenuation, *Limnol. Oceanogr.*, *55*(2), 703–713, doi:10.4319/lo.2009.55.2.0703.

Vivier, F., J. K. Hutchings, Y. Kawaguchi, T. Kikuchi, J. H. Morison, A. Lourenco, and T. Noguchi (2016), Sea ice melt onset associated with lead opening during the spring/summer transition near the North Pole, *J. Geophys. Res. Oceans*, *121*, 2499–2522, doi:10.1002/2015JC011588.

Walden, V. P., L. Cohen, S. Y. Murphy, S. R. Hudson, and M. A. Granskog (2017), Atmospheric components of the surface energy budget over young sea ice: Results from the N-ICE2015 campaign, *J. Geophys. Res. Atmos.*, doi:10.1002/2016JD026091.

Warren, S. G., and R. E. Brandt (2008), Optical constants of ice from the ultraviolet to the microwave: A revised compilation, *J. Geophys. Res.*, *113*, D14220, doi:10.1029/2007JD009744.

Willmes, S., and G. Heinemann (2016), Sea-ice wintertime lead frequencies and regional characteristics in the Arctic, 2003–2015, *Remote Sens.*, *8*(4), doi:10.3390/rs8010004.

Xie, H., C. Aubry, Y. Zhang, and G. Song (2014), Chromophoric dissolved organic matter (CDOM) in first-year sea ice in the western Canadian Arctic, *Mar. Chem.*, *165*, 25–35, doi:10.1016/j.marchem.2014.07.007.

Zeebe, R. E., H. Eicken, D. H. Robinson, D. Wolf-Gladrow, and G. S. Dieckmann (1996), Modeling the heating and melting of sea ice through light absorption by microalgae, *J. Geophys. Res.*, *101*(C1), 1163–1181, doi:10.1029/95JC02687.

Zudaire, L., and S. Roy (2001), Photoprotection and long-term acclimation to UV radiation in the marine diatom *Thalassiosira weissflogii*, *J. Photochem. Photobiol.*, *62*, 26–34, doi:10.1016/S1011-1344(01)00150-6.